Journal of Colloid and Interface Science 696 (2025) 137767

Contents lists available at ScienceDirect

Journal of Colloid And Interface Science

journal homepage: www.elsevier.com/locate/jcis

Regular Article

Mechanisms of interface jumps, pinning and hysteresis during cyclic fluid displacements in an isolated pore

Animesh Nepal [a], Juan J. Hidalgo [a], Jordi Ortín [b,c], Ivan Lunati [d], Marco Dentz [a,*]

[a] Spanish National Research Council (IDAEA-CSIC), C. Jordi Girona 18, 08034 Barcelona, Spain
[b] Departament de Física de la Matèria Condensada, Facultat de Física, Universitat de Barcelona, Martí i Franquès 1, 08028 Barcelona, Spain
[c] Universitat de Barcelona Institute of Complex Systems, Martí i Franquès 1, 08028 Barcelona, Spain
[d] EMPA, Swiss Federal Laboratories for Materials Science and Technology, Überlandstrasse 129, 8600, Dübendorf, Switzerland

GRAPHICAL ABSTRACT

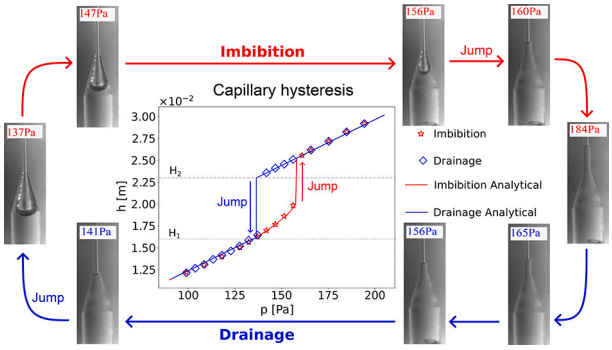

ARTICLE INFO

Keywords:
Capillary hysteresis
Interface pinning
Interface jump
Two-phase flow

ABSTRACT

Hypothesis: Quasi-static displacements of one immiscible fluid by another in a single pore can lead to interface jumps, pinning and capillary hysteresis, depending on the pore dimensions. It is expected that there is a critical pore configuration for which the interface becomes unstable and an interface jump is triggered. These processes are at the origin of hysteresis in porous media and control macroscopic two-phase fluid displacements.
Experiments and theory: We conduct quasi-static imbibition and drainage experiments and detailed numerical simulations in three and two-dimensional pores, represented by capillaries of different radii that are joined by a conical section (ink-bottle). A theoretical model for the interface is derived based on pressure balance that captures the full spectrum of possible interface behaviors.
Findings: Depending on the slope of the conical section, we observe a range of interfacial behaviors, including capillary jumps and interface pinning during both imbibition and drainage, which give rise to capillary hysteresis, that is, history dependence of the interface position. We identify a critical pore configuration for the occurrence of interface jumps and hysteresis, which depends on surface tension and contact angle.

* Corresponding author.
E-mail address: marco.dentz@csic.es (M. Dentz).

https://doi.org/10.1016/j.jcis.2025.137767
Received 1 January 2025; Received in revised form 29 April 2025; Accepted 30 April 2025
Available online 12 May 2025

1. Introduction

Cyclic two-phase flow in porous media, observed in various natural and industrial processes like carbon dioxide sequestration [1], underground hydrogen storage [2], enhanced oil recovery [3], and soil evaporation [4], is typically marked by pressure-saturation hysteresis. This means that the pressure required to achieve a given saturation during imbibition differs from that during drainage, resulting in different pressure-saturation trajectories [4]. During two-phase flow, the intrinsic pore-space variability in porous media leads to variability in interface curvature as the fluid-fluid interfaces move through the medium. This variability induces local interface instabilities that may align spatially, driving coordinated front movements (Haines jumps [5]), which are linked to energy dissipation [6,7]. Thus, local interface instabilities can be seen as the origin of capillary hysteresis in porous media [8–10].

Hysteresis models are typically constructed based on the general approach by Everett and Whitton [11], Preisach [12], and the mathematical descriptions provided by Krasnosel'skii and Pokrovskii [13], Mayergoyz [14], and Visintin [15], among others. These works propose that hysteresis arises from the presence of numerous independent domains within a system, some of which may exhibit metastability. These models are macroscopic and phenomenological, and account for the pore-scale processes that cause Haines jumps and interface pinning during imbibition and drainage by integrating factors such as pore geometry, connectivity, and fluid-solid interactions [16–20]. In this work, we focus on the detailed pore-scale processes that result in pressure-saturation hysteresis.

Haines jumps are ubiquitous for two-phase displacements in porous media and are caused by unstable interface configurations. These instabilities have a leading contribution to energy dissipation [7–9] and thus the efficiency of two-phase flow in porous media. They impact on fluid displacement patterns, are related to interface pinning, and are at the root of pressure-saturation hysteresis. Despite the central role of Haines jumps for the understanding of two-phase flow in porous media, their origin and impact on hysteresis is not well understood. In fact, while classical studies [6] refer to interface instability and unstable configuration, a quantitative description of the microscopic processes is often elusive. The imbibition experiments of Rubio et al. [21] in a thin two-dimensional porous medium show random interface pinning due to spatial variations in pore sizes and thus capillary forces, which they relate to the self-affine interface structure and scale-dependent scaling of its roughness. The experimental study Moebius and Or [22] evidences interfacial jumps and pinning during drainage in a porous medium. Both works emphasize the role of pore scale mechanisms for the macroscopic description of fluid displacement fronts in porous media. Koplik and Levine [23] use a stochastic interface model to elucidate the origin of interface pinning, namely the competition between the external driving force and capillary forces. The work by Sun and Santamarina [24] analyzes possible causes for Haines jumps in sinusoidal pores due to entrapped gas bubbles, compliant matrix, and interactions between connected pores. Following the seminal work of Joanny and De Gennes [25] for contact angle hysteresis, Planet et al. [26] and Holtzman et al. [10] study fluid displacement in Hele-Shaw cells characterized by variable aperture in order to assess the impact of capillary instabilities on hysteresis and energy dissipation [27]. However, the pore-scale mechanisms of Haines jumps in porous media and their geometrical controls remain open questions.

The spatial complexity of porous media complicates both experimental and numerical efforts to extract meaningful insights that can be molded into macroscopic descriptions of pressure-saturation hysteresis [28]. Thus, we focus here on imbibition and drainage in single pores, which can be represented by two capillaries of different radii that are connected by a conical section (ink-bottle), as shown in Fig. 1. Ferrari and Lunati [29] have used a similar setup to assess inertia effects during irreversible meniscus reconfiguration during imbibition into single pores with focus on corners. The study of simple geometries to obtain closed form solutions has provided insight into the sources of hysteresis, for example, in water retention, relative permeability, water freezing, or electrical resistivity curves [30,31].

Table 1
Fluid properties for the laboratory experiments.

μ_w	Silicone oil viscosity	0.0486 Pa s
ρ_w	Silicone oil density	972 kg m^{-3}
μ_{nw}	Air viscosity	1.48×10^{-5} Pa s
ρ_{nw}	Air density	1 kg m^{-3}
σ	Air-oil interfacial tension	0.0207 N m^{-1}
λ	Capillary length Eq. (1)	1.47 mm

The main objective of this work is to elucidate the influence of the pore geometry on capillary hysteresis during quasi-static imbibition and drainage. We disregard the impact of the roughness of the solid surface, which may give rise to contact angle hysteresis and interface pinning [25]. The specific research questions we are addressing are: Which conditions prompt the interface to jump during imbibition and drop during drainage, and how are these jumps and drops related to hysteresis? Which mechanism governs interface pinning during imbibition and drainage, and can we establish a predictive relationship to understand and quantify this phenomenon? In order to address these questions, we use laboratory experiments and numerical simulations to study imbibition, drainage and hysteresis in three and two spatial dimensions. The experimental and numerical observations are rationalized in a theoretical model.

2. Materials and methods

We present here the experimental, numerical and analytical methods that are used to study quasi-static imbibition and drainage in a single pore. The laboratory experiment uses a cylindrical ink-bottle setup and allows to explore a single parameter set. The numerical model, which is limited to two spatial dimensions due to computational complexity, is used to explore a wider parameter space and interfacial mechanisms. The analytical model provides a robust estimate of the interface position, and allows for an in-depth investigation and discussion of the mechanism of interface jumps, pinning and capillary hysteresis.

2.1. Laboratory experiment

The experiments consider imbibition and drainage in a vertical cylindrical ink-bottle under quasi-static conditions. A schematic of the experimental setup is shown in the Supplementary Material. The setup features an ink-bottle drilled into a clear acrylic rectangular prism and a wide cylindrical tube reservoir 28 mm in diameter) filled with silicone oil, which fully wets the walls of the ink-bottle and displaces the air initially present. Experiments were conducted at an ambient temperature of 23 °C. The fluid properties are listed in Table 1. The capillary length is defined by [32]

$$\lambda = \sqrt{\frac{\sigma}{\rho g}}, \tag{1}$$

where σ is surface tension, ρ fluid density and g gravity acceleration. It denotes the length at which capillary pressure balances hydrostatic pressure for a spherical droplet. For silicone oil it is $\lambda = 1.47$ mm. The Bond number is defined in terms of the radius of curvature of the fluid meniscus in a capillary with the capillary length as

$$\mathrm{Bo} = \frac{R^2}{\lambda^2} = \frac{\rho g R^2}{\sigma}, \tag{2}$$

where R is the radius of the capillary. The dimensions of the experimental ink-bottle are listed in Table 2. The radius of the lower tube corresponds to the size of a macropore or the pore size in coarse sand [33]. The radius of the upper tube to a typical pore size in a bead pack or

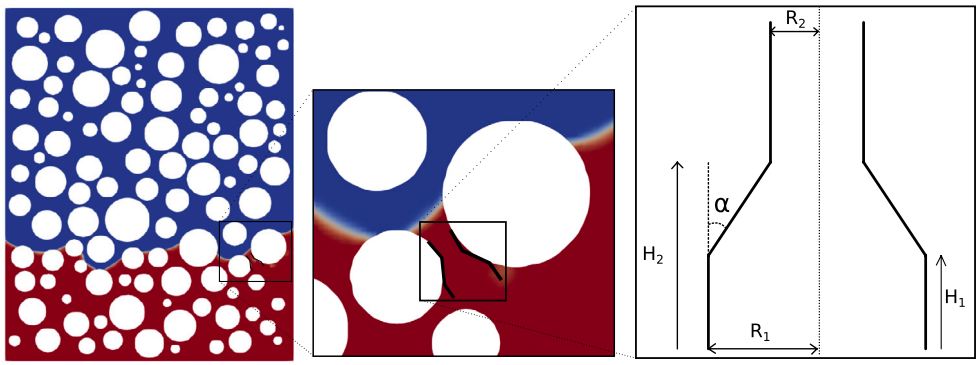

Fig. 1. Single pore-throat system in a porous medium resembling an ink-bottle. R_1 and R_2 are the radii of the lower and upper cylindrical tubes, respectively. H_1 is the height of the upper end of the lower tube, while H_2 is the height of lower end of the upper tube, and α is the angle of the conical section.

Table 2
Experimental ink-bottle parameters.

θ	Contact angle	0°
α	Angle of conical section	15°
R_1	Lower radius	2.3 mm
R_2	Upper radius	0.5 mm
H_1	Height of upper end of lower tube	16 mm
H_2	Height of lower end of upper tube	23 mm

Table 3
Numerical ink-bottle parameters.

θ	Contact angle	45°
R_1	Lower radius	0.5 mm
R_2	Upper radius	0.35 mm
H_1	Height of upper end of lower tube	8 mm

medium sand [34]. The Bond number for the lower capillary tube is Bo = 2.44, and for the upper capillary tube Bo = 0.12. Thus, the fluid meniscus in the lower tube is deformed by gravity. In the upper tube, capillary pressure is dominant and the meniscus has the form of a spherical cap.

The reservoir was mounted on a platform that can be adjusted to change the inlet pressure, measured by a displacement gauge with a sensitivity of 0.01 mm. During imbibition, the platform is raised incrementally to increase the inlet pressure, allowing fluid to enter the ink-bottle, and the system is allowed to equilibrate at each step for at least 10 min. During drainage, this procedure is reversed. The setup was backlit, and a camera with a macro lens captured images at each pressure step, which were analyzed using the Python library cv2 [35].

2.2. Numerical simulations

We perform numerical simulations of immiscible displacement of one incompressible fluid by another under isothermal conditions and quasi-static driving in a two-dimensional setup, complementary to the three-dimensional experimental setting described in the previous section. The numerical model solves a set of continuity and momentum balance equations for pressure and velocity fields in the whole domain. In order to track the interface between the two fluids, we use the volume of fluid (VOF) approach [36]. The surface tension force in the momentum balance equation is described by the continuum surface force (CSF) model [37]. In this model, the curvature of the interface is approximated by the divergence of the unit normal to the interface, which can be expressed as the norm of the gradient of the volume fraction term used in the VOF method. Further details on the governing equations, VOF approach and CSF model are given in the Supplementary Material. The numerical simulations are run in OpenFOAM [38]. Continuity and momentum balance equations are solved using a finite volume method on a grid with an accuracy of first order in time and second order in space. The two-dimensional computational domain of the ink-bottle is discretized with the mesh consisting of uniform hexahedral cells with 0.05 mm side lengths.

The fluid properties are the same as in the experiment and listed in Table 1. The dimensions of the numerical ink-bottle are given in Table 3. Note that the radii R_1 and R_2 of the lower and upper tube as well as the height H_1 of the lower tube are fixed. We vary the angle α of the conical section and thus the height H_2 according to $H_2 = H_1 + (R_1 - R_2)\tan(\alpha)$. The tube radii correspond to typical pore sizes in bead packs and medium sands [34]. The capillary length is the same as for the experiment, $\lambda = 1.45$ mm. However, the Bond numbers in the lower and upper tubes are Bo = 0.12 and 0.06. That is, the meniscus shape in both tubes is capillary dominated.

A no-slip boundary condition is applied to the walls, along with a specified contact angle. Pressure boundary conditions are set at the inlet and outlet of the ink-bottle. Pressure at the inlet is increased (imbibition) or decreased (drainage) at a regular interval of 2 s allowing the fluid to equilibrate. The time interval between pressure increments is determined from a previous simulation run, where the simulation was conducted in a straight capillary tube until the fluid equilibrated with the applied external pressure.

2.3. Analytical model for interface height

In this section, we develop an analytical model for the interface height during pressure-driven quasi-static imbibition and drainage in an ink-bottle. The ink-bottle is divided into three sections. The first section comprises the lower tube of radius R_1, the third section the upper tube of radius $R_2 < R_1$. The second section is the conical section that connects the upper and lower tubes. For an illustration, see Fig. 1 and the Supplementary Material. For each section, we derive the equilibrium interface height separately by using the balance between hydrostatic pressure, external pressure p, and capillary pressure p_c,

$$\rho g h = p + p_c. \tag{3}$$

Capillary pressure is given by the Young-Laplace equation, which for a tube with a circular cross section of radius R reads as

$$p_c = \frac{2\sigma}{R_c}. \tag{4}$$

Surface tension is denoted by σ and R_c denotes the radius of curvature of the interface. For a straight tube, R_c is given by

$$R_c = \frac{R}{\cos(\theta)}, \tag{5}$$

where θ is the equilibrium contact angle and R the tube radius.

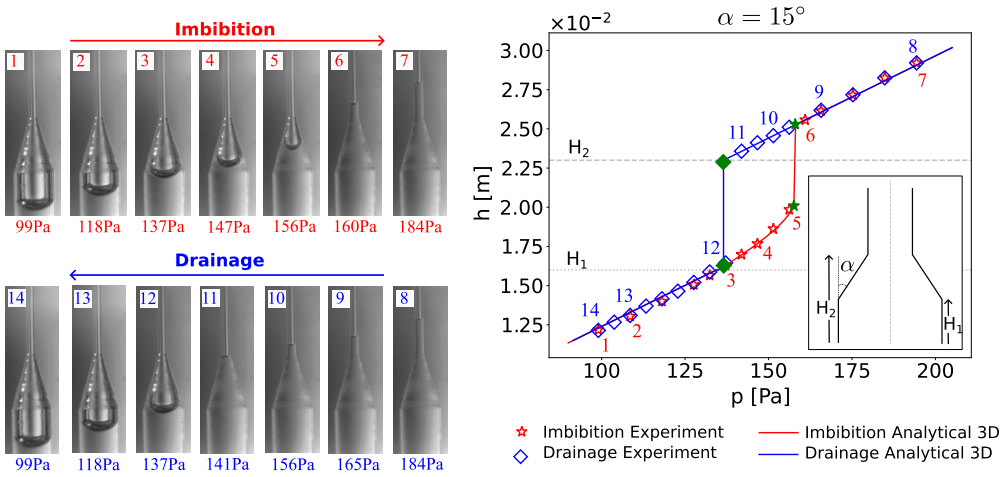

Fig. 2. Left panel: Experimental meniscus images at varying external pressures for $\alpha = 15°$ and $\theta = 0°$, with remaining parameters detailed in Table 2. The label beneath each image indicates the pressure difference between the inlet and outlet. Right panel: Interface height as a function of the external pressure. Red star markers indicate experimental imbibition data points, while blue diamond markers represent experimental drainage data points. Numbered markers correspond to meniscus images in the left panel. The red line represents the analytical interface heights derived in Section 2.3 for (blue) imbibition and (red) drainage. Vertical lines connecting green markers indicate Haines jumps, which occur at different external pressure during imbibition and drainage, thus resulting in hysteresis. Two dotted horizontal lines are H_1 and H_2. (For interpretation of the colors in the figure(s), the reader is referred to the web version of this article.)

2.3.1. Section 1: $h < H_1$

From Equations (3) to (5), we obtain the interface height

$$h = \frac{p}{\rho g} + \frac{2\sigma\cos(\theta)}{\rho g R_1}, \tag{6}$$

where R_1 is the radius of the lower tube. This expression is known as the Jurin height [39].

2.3.2. Section 2: $H_1 < h < H_2$

In the conical section, the inclination of the walls and the decrease in radius lead in general to an increase of the interface curvature compared to Section 1. In fact, the radius of curvature is

$$R_c(h) = \frac{R(h)}{\cos(\theta - \alpha)}, \tag{7}$$

where α is the angle between the wall of the conical section and the vertical, and $R(h) = R_1 - (h - H_1)\tan(\alpha)$ is the radius at height h, see the Supplementary Material. Thus, we obtain for the interface height the implicit equation

$$h = \frac{p}{\rho g} + \frac{2\sigma\cos(\theta - \alpha)}{\rho g\left[R_1 - (h - H_1)\tan(\alpha)\right]}, \tag{8}$$

which is quadratic in h.

2.3.3. Section 3: $h > H_2$

In the third, straight section, the expression for the interface height is

$$h = \frac{p}{\rho g} + \frac{2\sigma\cos(\theta)}{\rho g R_2}, \tag{9}$$

where R_2 is the radius of the upper tube. The expressions for two dimensions can be derived in full analogy to three dimensions with the only difference that capillary pressure is $p_c = \sigma/R_c$.

3. Results

3.1. Experimental results

The fluid properties and dimensions for the experimental ink-bottle are given in Table 1 and Table 2. Fig. 2 shows the experimental data for the interface height at different external pressures as well as the analytical results for the interface height presented in Section 2.3. Note that the analytical expressions are derived based on the assumption that the tube radii are smaller than the capillary length, which however is not the case in the lower tube. Nevertheless, firstly, the capillary rise in the lower tube is small compared to the height of the oil column due to the external pressure, and secondly, the non sphericity has only a minor effect on the interface position estimated by the Young-Laplace equation [40]. For the upper tube in contrast, the radius is less the half of λ and capillarity dominates. In both the upper and lower tube, the interface height varies linearly and reversibly with external pressure during cyclic imbibition and drainage. This behavior is correctly described by the analytical expressions of Section 2.3 for which no fitting parameters are used. During imbibition, the interface enters the conical section smoothly with increasing external pressure up to a certain height for which $p = 160$ Pa, at which a Haines jump occurs into the upper tube. During drainage, the interface falls at external pressure $p = 137$ Pa through the conical section from H_2 to H_1. The pressure-height data exhibits hysteresis because the interface jumps occur at different external pressure, which is correctly captured by the analytical interface model.

3.2. Simulation results

We simulate cyclic imbibition-drainage in three different two-dimensional ink-bottles with different cross-section gradients, hence different angles of the conical section. We choose the angles α and the contact angle θ different from those used in the experiment in order to explore a wider range of interface behaviors beyond the experimental observations. The resulting interface height is plotted as a function of pressure in Fig. 3 for $\alpha = 10°, 6°$ and $2°$ with contact angle $\theta = 45°$. The interface heights during imbibition and drainage are linearly dependent on the external pressure in the lower and upper tubes for all three ink-bottles. For $\alpha = 10°$ and $6°$, Haines jumps are observed at height H_1 during imbibition and at height H_2 during drainage. These jumps occur at different external pressures, which results in hysteresis. Unlike in the experiments, we observe interface pinning at height H_2 during both imbibition and drainage for $\alpha = 6°$, but only during drainage for $\alpha = 10°$, as shown in Fig. 3. This is marked by the nearly horizontal line at height H_2. For $\alpha = 2°$, there is no Haines jump or interface pinning anywhere in the ink-bottle. The $h - p$ trajectory is fully reversible. Thus, there seems to be a critical angle between $\alpha = 6°$ and $2°$ that separates hysteretic from non-hysteretic behavior of the interface.

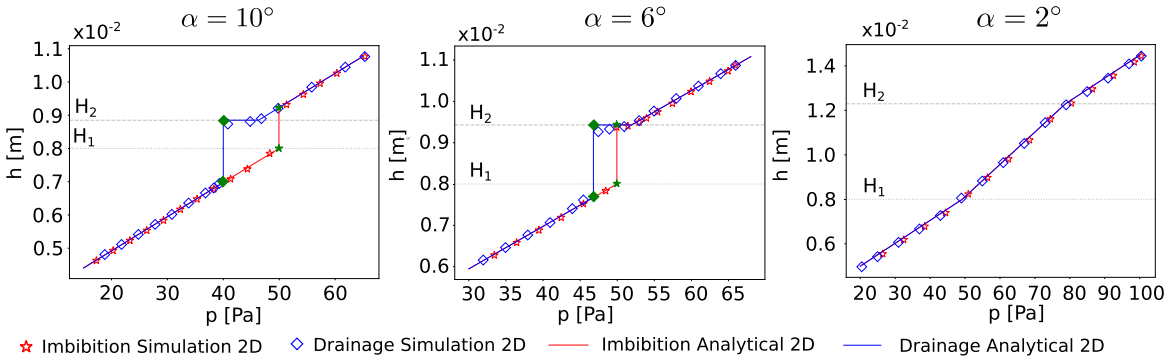

Fig. 3. Simulated interface heights versus external pressure for two-dimensional ink bottles with $\alpha = 10°$, 6°, and 2°, and $\theta = 45°$. The remaining parameters are detailed in Table 2. Red star markers indicate simulation imbibition data points, while blue diamond markers represent simulation drainage data points. The red line represents analytical interface heights during imbibition, derived in section 4.1.1, and the blue line shows those during drainage, derived in section 4.1.2. Vertical lines connecting green markers indicate Haines jumps for $\alpha = 10°$ and 6°, which occur at different external pressures during imbibition and drainage, thus resulting in hysteresis. For $\alpha = 2°$, the h-p trajectory is fully reversible. The two dotted horizontal lines represent H_1, fixed at 8 mm, and $H_2 = H_1 + (R_1 - R_2)/\tan(\alpha)$.

4. Theory and discussion

In this section, we use the analytical model for the interface position presented in Section 2.3 to develop a theory for the mechanisms of hysteresis in a single pore. We discuss the evolution of the interface position during imbibition and drainage cycles in the light of the theoretical findings and analyze the mechanisms that lead to capillary hysteresis and interface pinning. The theory identifies the critical angles for the occurrence of hysteresis and interface pinning at the conical section, which is corroborated by the experimental and numerical data.

4.1. Mechanisms of imbibition and drainage

We identify and discuss the criteria under which the interface can jump or get pinned. To this end, we focus on the processes at the beginning, within, and at the end of the conical section.

4.1.1. Imbibition

As the external pressure increases, the interface rises to a height H_1 with pressure

$$p_{H_1} = \rho g H_1 - \frac{2\sigma\cos(\theta)}{R_1}. \tag{10}$$

At height H_1, the interface is unstable because it changes its curvature from $\cos(\theta)/R_1$ to $\cos(\theta-\alpha)/R_1$ upon an infinitesimal change of external pressure. In the conical section, the interface height h for p_{H_1} and curvature $\cos(\theta-\alpha)/R_1$ is

$$h = \frac{p_{H_1}}{\rho g} + \frac{2\sigma\cos(\theta-\alpha)}{\rho g R_1} = H_1 + \frac{2\sigma[\cos(\theta-\alpha)-\cos(\theta)]}{\rho g R_1}. \tag{11}$$

For $\alpha < 2\theta$, h is larger than H_1 because the radius of curvature is smaller and thus capillary pressure is larger than in the lower straight tube. Hence, the interface jumps into the conical section. For $\alpha > 2\theta$, h would be smaller than H_1 because the radius of curvature is larger than in the lower tube. Consequently, the interface is pinned at H_1. The pinned interface is mobilized when the external pressure reaches

$$p_1 = \rho g H_1 - \frac{2\sigma\cos(\theta-\alpha)}{R_1}. \tag{12}$$

For the experiments discussed in Section 2.1 the contact angle is $\theta = 0°$, that is, the interface is always pinned at H_1. However, the pressure differential required to mobilize the interface is too small to be visible in Fig. 2. For the numerical simulations, $\theta = 45°$, that is $\alpha < 2\theta$ and therefore the interface cannot be pinned at H_1.

The position of the interface in the conical section is obtained from the solution of the quadratic Equation (8) for $p \geq p_{H_1}$ as

$$h_{\pm} = \frac{p\tan(\alpha) + \rho g H_1\tan(\alpha) + \rho g R_1}{2\rho g\tan(\alpha)} \pm \sqrt{\Delta}, \tag{13}$$

where the discriminant Δ is given by

$$\Delta = \left[\frac{p\tan(\alpha) + \rho g H_1\tan(\alpha) + \rho g R_1}{2\rho g\tan(\alpha)}\right]^2 - \frac{2\sigma\cos(\theta-\alpha) + p[R_1 + H_1\tan(\alpha)]}{\rho g\tan(\alpha)}. \tag{14}$$

If the discriminant is negative for a given $p \geq p_{H_1}$, the solution is not a real number, which indicates a jump. We define the critical angle α_k as the angle α of the conical section for which $\Delta = 0$ for fixed $p = p_{H_1}$ in Equation (14). Therefore, the interface jumps at H_1 for $\alpha \geq \alpha_k$. If $\alpha < \alpha_k$, the discriminant is positive for $p = p_{H_1}$ and the interface moves smoothly into the conical section. The equilibrium heights are given by $h = h_+$ in Equation (13). The interface advances with increasing external pressure up to a critical height h_k, at which the curvature is large enough to trigger a runaway event. For a given angle $\alpha < \alpha_k$, the height h_k can be determined by (i) setting $\Delta = 0$ in Equation (14) and solving for p, which gives the critical external pressure p_k, and (ii) inserting p_k into Equation (13), which yields

$$h_k = \frac{p_k\tan(\alpha) + \rho g H_1\tan(\alpha) + \rho g R_1}{2\rho g\tan(\alpha)}. \tag{15}$$

At $h = h_k$, the interface jumps. If $h_k > H_2$, the interface moves smoothly up to the end of the conical section.

In the laboratory experiments $\alpha < \alpha_k \approx 89°$. Thus, the interface moves into the conical section and jumps at a critical height and pressure as shown in Fig. 2. In the numerical simulations shown in Fig. 3, $\alpha_k \approx 5.28°$. For $\alpha > \alpha_k$, the interface jumps from H_1 across the whole conical section. The intersection of p_k with the line p_{H_2} marks the angle α_0 below which no jumps can be observed. The angle below which no jump occurs in the experiment is $\alpha_0 = 3.27°$, and for the simulations it is $\alpha_0 = 5.28°$, which coincides with α_k.

When the runaway event is triggered at external pressure p_k, the interface may (i) jump into the upper straight section, or (ii) jump to the height $h = H_2$ and get pinned, depending on the interface curvature at $h = H_2$. At $h = H_2$, the interface is metastable regarding the two curvatures $\cos(\theta-\alpha)/R_2$ and $\cos(\theta)/R_2$. If the critical external pressure is

$$p_k > p_{H_2} = \rho g H_2 - \frac{2\sigma\cos(\theta)}{R_2} \tag{16}$$

the interface advances into the upper straight section up to the height

$$h = \frac{p_k}{\rho g} + \frac{2\sigma\cos(\theta)}{\rho g R_2}. \tag{17}$$

If on the other hand $p_k < p_{H_2}$, the interface is pinned. It is mobilized at the external pressure $p = p_{H_2}$. In the straight upper tube, the interface then advances according to Equation (9). These behaviors are illustrated in Figs. 2 and 3. In the experiments, the interface jumps into the upper tube from a critical height h_k because $p_k > p_{H_2}$. In the numerical simulations, for $\theta = 45°$, $p_k = p_{H_1}$. Here we observe pinning at H_2 for $\alpha = 6°$.

4.1.2. Drainage

During drainage, the interface height decreases linearly with the external pressure according to Equation (9) until it arrives at $h = H_2$ for $p = p_{H_2}$. At $h = H_2$, the curvature changes from $R_2/\cos(\alpha)$ to $R_2/\cos(\theta - \alpha)$ upon an infinitesimal decrease of external pressure, and the interface height is

$$h = \frac{p_{H_2}}{\rho g} + \frac{2\sigma\cos(\theta-\alpha)}{\rho g R_2} = H_2 + \frac{2\sigma[\cos(\theta-\alpha)-\cos(\theta)]}{\rho g R_2}. \tag{18}$$

For $\alpha > 2\theta$, the new interface height is $h < H_2$ because the new capillary pressure cannot sustain the liquid column. If $p_{H_2} > p_{H_1}$ the interface drops to a new equilibrium position inside the conical section. For $p_{H_2} \le p_{H_1}$ it drops to or beyond H_1. For $\alpha < 2\theta$, h would be larger than H_2. Consequently, the interface is pinned at H_2. It is unpinned at the external pressure

$$p_2 = \rho g H_2 - \frac{2\sigma\cos(\theta-\alpha)}{R_2}, \tag{19}$$

and drops to a new interface height either in the conical section or the lower straight tube depending on whether p_2 is larger or smaller than p_{H_1}. This interface pinning at a sharp edge is related to apparent contact angle hysteresis. As discussed in the review paper by Quéré [41] for a drop moving over a straight horizontal surface with a groove, one observes a contact angle θ before the edge and an apparent contact angle $\alpha + \theta$ (referred to the horizontal) after the edge. Note that we use here the angle convention of Fig. 1. Thus, at the groove the interface can be pinned as if the apparent surface were non-wetting. The expanding conical section has a similar effect for the advancing interface, but here we need to account also for the change of the interface curvature and its effect on capillary pressure. Thus, we find, as pointed out above, that pinning occurs only if α is smaller than the critical angle 2θ. In the experiments, the interface is not pinned and drops as it arrives at H_2 because $\theta = 0°$, see Fig. 2. In the numerical simulations $\theta = 45°$. As $\alpha < 2\theta$, in all cases, the interface is always pinned as illustrated in Fig. 3.

4.2. Energy density of the fluid interface

To further illustrate how the metastability of the interface in the conical section affects imbibition and drainage, we define the energy function

$$U(z) = -\int_0^z dz' p_e(z'), \tag{20}$$

where the effective pressure $p_e(z)$ is defined by

$$p_e(z) = \rho g(z - h_e) - p_c(z). \tag{21}$$

The external head is $h_e = p/\rho g$. According to (5), the capillary pressure is $p_c(z) = 2\sigma/R_c(z)$, where $R_c(z) = R_1/\cos(\theta)$ and $R_c(z) = R_2/\cos(\theta)$ in the lower and upper sections, and according to (7) it is $R_c = [R_1 - (z - H_1)\tan\alpha]/\cos(\theta - \alpha)$ in the conical section. By definition, the minima of $U(z)$ determine the interface position h, that is,

$$-\left.\frac{dU(z)}{dz}\right|_{z=h} = p_e(z=h) = 0. \tag{22}$$

Using Equations (20) and (21), we obtain for $0 < z < H_1$

$$U(z) = \frac{1}{2}\rho g(h-h_e)^2 - \frac{1}{2}\rho g h_e^2 - \frac{2\sigma\cos(\theta)}{R_1}h. \tag{23}$$

For $H_1 < z < H_2$, the energy function reads

$$U(z) = \frac{1}{2}\rho g(h-h_e)^2 - \frac{1}{2}\rho g h_e^2 - \frac{2\sigma\cos(\theta)}{R_1}H_1 - \frac{2\sigma\cos(\theta-\alpha)}{\tan(\alpha)}\ln\left[\frac{R_1}{R_1-(h-H_1)\tan(\alpha)}\right] \tag{24}$$

And for $z > H_2$ we obtain

$$U(z) = \frac{1}{2}\rho g(h-h_e)^2 - \frac{1}{2}\rho g h_e^2 - \frac{2\sigma\cos(\theta)}{R_1}H_1 - \frac{2\sigma\cos(\theta-\alpha)}{\tan(\alpha)}\ln\left[\frac{R_1}{R_1-(H_2-H_1)\tan(\alpha)}\right] - \frac{2\sigma\cos(\theta)}{R_2}(h-H_2). \tag{25}$$

Fig. 4 shows the energy functions corresponding to the numerical simulations for $\alpha = 10°$ and to the experiment for $\alpha = 15°$. The symbols denote the possible interface positions corresponding to local energy minima. There is a single energy minimum when the interface is in the lower tube or upper tube. In the vicinity of the beginning and end of the conical section the energy density can become metastable depending on the external pressure. For the numerical simulations with $\alpha = 10°$, the energy develops a saddle point at p_{H_1} and the interface becomes unstable. It jumps to the local minimum at $z > H_2$. During drainage, the interface is pinned at $z = H_2$ because the local energy minimum at $z = H_2$ is not unstable. The interface becomes unstable only when the external pressure is lowered further, which is when it drops below the conical section. For the experimental interface heights with $\alpha = 15°$, the energy has a single minimum when the interface reaches $z = H_1$ at p_{H_1}. Only when the external pressure is increased to p_k does the minimum become unstable. The interface then can jump to the new energy minimum at $z > H_2$. During drainage, the interface is not pinned at $z = H_2$, it becomes unstable and drops to $z \approx H_1$.

5. Conclusions

It has been known for a century that interface instabilities and pinning are key mechanisms for fluid displacements in porous media [6,17,42], but the underlying pore-scale mechanisms have been elusive. In this work, we have studied how the geometry of a single pore can control the displacements of two immiscible fluids, and how it is related to capillary hysteresis, interface jumps and pinning. Experiments and numerical simulations have shown that there is a critical shape for which the interface becomes unstable, interface jumps are triggered and hysteresis ensues. A theoretical model captures the full spectrum of possible interface configurations, and elucidates the mechanisms of imbibition and drainage. The theory relates the critical angle α_k of the pore constriction to contact angle and surface tension between the two fluids and explains observed interface pinning during imbibition and drainage. These results show that a single pore features the fundamental mechanisms leading to Haines jumps and hysteresis without additional effects such as compliance of the solid matrix, trapped gas bubbles, or interconnected capillaries [22,24]. The geometry under consideration, connected pores of different radii can be ubiquitously found in natural and industrial porous media [34], which makes the reported results relevant for a wide range of porous media applications. In this paper we have focused on one aspect of hysteresis, namely capillary hysteresis. For example wettability variability and surface roughness can give rise to contact angle hysteresis [43], which is another source for hysteresis in porous media.

The critical angle α_k defines the transition between two different types of interface motion. For $\alpha < \alpha_k$, the interface moves smoothly through the conical section, whereas for $\alpha > \alpha_k$ the interface exhibits metastable behavior that leads to interface jumps and hysteresis. The magnitude of the jump and the size of the hysteresis cycle increase with increasing α. Depending on the angle α, surface tension σ and contact angle θ, the interface may jump and get pinned at the end of the conical

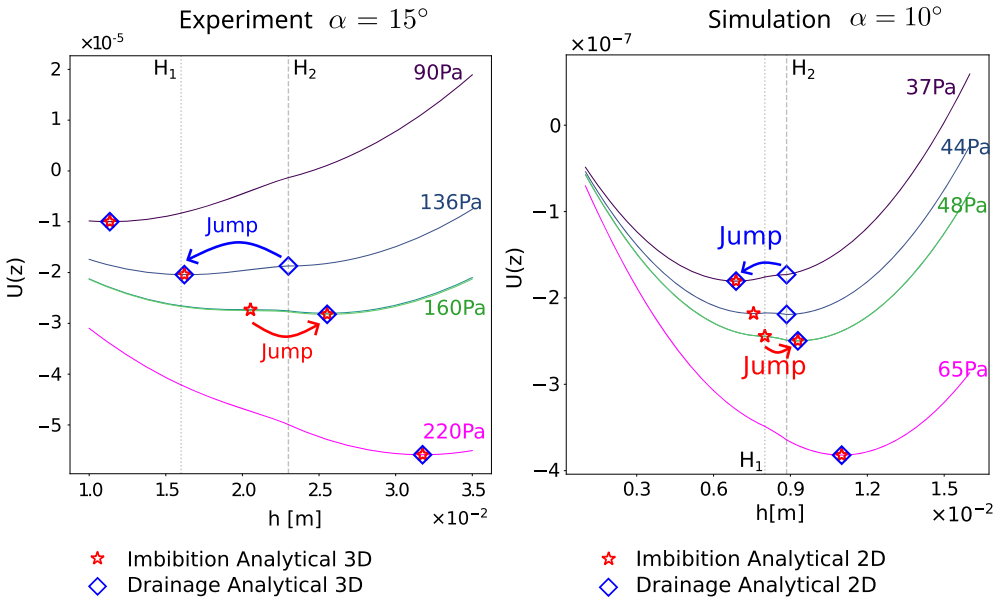

Fig. 4. Energy functions for various external pressures, illustrating energy minima corresponding to the interface height. Red and blue markers show the analytical interface heights during imbibition and drainage, respectively. Vertical dotted lines represent heights H_1 and H_2. The left panel corresponds to the interfaces shown in Fig. 2, the right panel to the interfaces shown in the left panel of Fig. 3.

section, which occurs if the external pressure cannot sustain the interface in the upper capillary during imbibition. On the other hand, if the external pressure at the jump is larger than what is required to sustain the interface at the upper end of the capillary, the interface jumps beyond it. During drainage, the interface is pinned at the upper end of the conical section if the contact angle is $\theta < \alpha/2$. In this case, the external pressure is larger than what is required to hold the interface. Further lowering the external pressure increases the interface curvature, which eventually leads to the release of the interface. For $\theta > \alpha/2$, the interface drops when it reaches the upper end of the conical section. The pore geometry, contact angle and surface tension are the key parameters for the occurrence of Haines jumps and hysteresis.

These results show possible ways for the control of energy dissipation and hysteresis, and thus displacement efficiency. In fabricated porous media this can be achieved through the design of individual pore shapes as a function of the fluid properties. In natural porous media, for which the pore space cannot be modified, this can be realized through manipulation of wettability and surface tension. Furthermore, our findings provide new insights into the role of pore geometry for the implementation of two-phase flow in pore network models [44–46], and how to account for pore-scale variability in discrete-domain models for multiphase flow and hysteresis in porous media [9]. It remains to be explored how dynamic effects and inertia [22,29] impact on or possibly alter these processes, and how individual pores respond in a connected network of pores with different geometrical properties [47]. Also the roughness of the pore surface may alter the observed behaviors because it can give rise to additional interface pinning through contact angle hysteresis [25]. The presented results can provide the basis for future studies into the role and control of pore scale processes and heterogeneity on macroscopic fluid displacements, and the generation of displacement patterns.

CRediT authorship contribution statement

Animesh Nepal: Writing – review & editing, Writing – original draft, Software, Methodology, Investigation, Formal analysis, Conceptualization. **Juan J. Hidalgo:** Writing – review & editing, Writing – original draft, Software, Methodology, Investigation, Funding acquisition, Formal analysis. **Jordi Ortín:** Writing – review & editing, Supervision, Investigation, Formal analysis, Conceptualization. **Ivan Lunati:** Writing – review & editing, Software, Methodology, Formal analysis. **Marco Dentz:** Writing – review & editing, Writing – original draft, Supervision, Resources, Project administration, Methodology, Investigation, Funding acquisition, Formal analysis, Conceptualization.

Declaration of competing interest

The authors declare that they have no known competing financial interests or personal relationships that could have appeared to influence the work reported in this paper.

Acknowledgements

The authors acknowledge the support from Spanish State Research Agency (10.13039/501100011033) and Spanish Ministry of Science and Innovation through the projects HydroPore (PID2019-106887GB-C31 and C32) and HydroPore II (PID2022-137652NB-C41 and C42). JO acknowledges AGAUR for partial financial support under grant 2021-SGR-00450.

Appendix A. Supplementary material

Supplementary material related to this article can be found online at https://doi.org/10.1016/j.jcis.2025.137767.

Data availability

Data will be made available on request.

References

[1] A. Cihan, S. Wang, T.K. Tokunaga, J.T. Birkholzer, The role of capillary hysteresis and pore-scale heterogeneity in limiting the migration of buoyant immiscible fluids in porous media, Water Resour. Res. 54 (2018) 4309.
[2] L. Hashemi, M. Blunt, H. Hajibeygi, Pore-scale modelling and sensitivity analyses of hydrogen-brine multiphase flow in geological porous media, Sci. Rep. 11 (2021) 8348.
[3] M. Sahimi, Flow and Transport in Porous Media and Fractured Rock: from Classical Methods to Modern Approaches, John Wiley & Sons, 2011.
[4] B. Albers, Modeling the hysteretic behavior of the capillary pressure in partially saturated porous media: a review, Acta Mech. 225 (2014) 2163.

[5] W.B. Haines, Studies in the physical properties of soils: IV. A further contribution to the theory of capillary phenomena in soil, J. Agric. Sci. 17 (1927) 264.
[6] N.R. Morrow, Physics and thermodynamics of capillary action in porous media, Ind. Eng. Chem. 62 (1970) 32.
[7] S. Berg, H. Ott, S.A. Klapp, A. Schwing, R. Neiteler, N. Brussee, A. Makurat, L. Leu, F. Enzmann, J.-O. Schwarz, et al., Real-time 3d imaging of haines jumps in porous media flow, Proc. Natl. Acad. Sci. 110 (2013) 3755.
[8] S. Schlüter, S. Berg, M. Rücker, R. Armstrong, H.-J. Vogel, R. Hilfer, D. Wildenschild, Pore-scale displacement mechanisms as a source of hysteresis for two-phase flow in porous media, Water Resour. Res. 52 (2016) 2194.
[9] L. Cueto-Felgueroso, R. Juanes, A discrete-domain description of multiphase flow in porous media: rugged energy landscapes and the origin of hysteresis, Geophys. Res. Lett. 43 (2016) 1615.
[10] R. Holtzman, M. Dentz, R. Planet, J. Ortín, The origin of hysteresis and memory of two-phase flow in disordered media, Commun. Phys. 3 (2020) 222.
[11] D.H. Everett, W.I. Whitton, A general approach to hysteresis, Trans. Faraday Soc. 48 (1952) 749.
[12] F. Preisach, Über die magnetische nachwirkung, Z. Phys. 94 (1935) 277.
[13] M.A. Krasnosel'skii, A.V. Pokrovskii, Systems with Hysteresis, Springer Science & Business Media, 2012.
[14] I. Mayergoyz, Mathematical models of hysteresis, IEEE Trans. Magn. 22 (1986) 603.
[15] A. Visintin, Differential Models of Hysteresis, vol. 111, Springer Science & Business Media, 2013.
[16] A. Poulovassilis, Hysteresis of pore water, an application of the concept of independent domains, Soil Res. 93 (1962) 405.
[17] Y. Mualem, A conceptual model of hysteresis, Water Resour. Res. 10 (1974) 514.
[18] A.Y. Beliaev, S.M. Hassanizadeh, A theoretical model of hysteresis and dynamic effects in the capillary relation for two-phase flow in porous media, Transp. Porous Media 43 (2001) 487.
[19] R. Hilfer, Capillary pressure, hysteresis and residual saturation in porous media, Phys. A, Stat. Mech. Appl. 359 (2006) 119.
[20] R. Hilfer, Macroscopic capillarity and hysteresis for flow in porous media, Phys. Rev. E 73 (2006) 016307.
[21] M.A. Rubio, C.A. Edwards, A. Dougherty, J.P. Gollub, Self-affine fractal interfaces from immiscible displacement in porous media, Phys. Rev. Lett. 63 (1989) 1685.
[22] F. Moebius, D. Or, Interfacial jumps and pressure bursts during fluid displacement in interacting irregular capillaries, J. Colloid Interface Sci. 377 (2012) 406.
[23] J. Koplik, H. Levine, Interface moving through a random background, Phys. Rev. B 32 (1985) 280.
[24] Z. Sun, J.C. Santamarina, Haines jumps: pore scale mechanisms, Phys. Rev. Lett. 100 (2019) 023115.
[25] J. Joanny, P.-G. De, Gennes, a model for contact angle hysteresis, J. Chem. Phys. 81 (1984) 552.
[26] R. Planet, L. Díaz-Piola, J. Ortín, Capillary jumps of fluid-fluid fronts across an elementary constriction in a model open fracture, Phys. Rev. Fluids 5 (2020) 044002.
[27] R. Holtzman, M. Dentz, R. Planet, J. Ortín, The relation between dissipation and memory in two-fluid displacements in disordered media, Geophys. Res. Lett. 50 (2023) e2023GL104073.
[28] A. Ferrari, J. Jimenez-Martinez, T.L. Borgne, Y. Méheust, I. Lunati, Challenges in modeling unstable two-phase flow experiments in porous micromodels, Water Resour. Res. 51 (2015) 1381.
[29] A. Ferrari, I. Lunati, Inertial effects during irreversible meniscus reconfiguration in angular pores, Adv. Water Resour. 74 (2014) 1.
[30] L. Guarracino, T. Rötting, J. Carrera, A fractal model to describe the evolution of multiphase flow properties during mineral dissolution, Adv. Water Resour. 67 (2014) 78.
[31] H. Luo, D. Jougnot, A. Jost, J.K. Limbrock, S. Wang, L.D. Thanh, A. Kemna, Bayesian inference of hysteretic behavior of unfrozen water content and electrical conductivity in saturated frozen rocks, J. Hydrol. 645 (2024) 132146.
[32] P.-G. De Gennes, F. Brochard-Wyart, D. Quéré, Capillarity and Wetting Phenomena: Drops, Bubbles, Pearls, Waves, Springer Science & Business Media, 2003.
[33] G. Warner, J. Nieber, I. Moore, R.A. Geise, Characterizing macropores in soil by computed tomography, Soil Sci. Soc. Am. J. 53 (1989) 653.
[34] F.A. Dullien, Porous Media: Fluid Transport and Pore Structure, Academic Press, 2012.
[35] G. Bradski, The OpenCV library, Dr. Dobb's J. Softw. Tools (2000).
[36] C.W. Hirt, B.D. Nichols, Volume of fluid (vof) method for the dynamics of free boundaries, J. Comput. Phys. 39 (1981) 201.
[37] J.U. Brackbill, D.B. Kothe, C. Zemach, A continuum method for modeling surface tension, J. Comput. Phys. 100 (1992) 335.
[38] OpenFOAM Foundation, OpenFOAM: the open source CFD toolbox, available at https://openfoam.org, 2023.
[39] J. Jurin, II. An account of some experiments shown before the royal society; with an enquiry into the cause of the ascent and suspension of water in capillary tubes, Philos. Trans. R. Soc. Lond. 30 (1718) 739.
[40] S. Liu, S. Li, J. Liu, Jurin's law revisited: exact meniscus shape and column height, Eur. Phys. J. E 41 (2018) 1.
[41] D. Quéré, Wetting and roughness, Annu. Rev. Mater. Res. 38 (2008) 71.
[42] W.B. Haines, Studies in the physical properties of soil. V. The hysteresis effect in capillary properties, and the modes of moisture distribution associated therewith, J. Agric. Sci. 20 (1930) 97.
[43] K.-Y. Law, Contact angle hysteresis on smooth/flat and rough surfaces. Interpretation, mechanism, and origin, Acc. Mater. Res. 3 (2021) 1.
[44] V. Joekar-Niasar, S. Hassanizadeh, Analysis of fundamentals of two-phase flow in porous media using dynamic pore-network models: a review, Crit. Rev. Environ. Sci. Technol. 42 (2012) 1895.
[45] M. Regaieg, A. Moncorgé, Adaptive dynamic/quasi-static pore network model for efficient multiphase flow simulation, Comput. Geosci. 21 (2017) 795.
[46] F. Moebius, D. Or, Inertial forces affect fluid front displacement dynamics in a pore-throat network model, Phys. Rev. E 90 (2014) 023019.
[47] R. Das, V.S. Deshpande, N.A. Fleck, Capillary rise in a packing of glass spheres, J. Mech. Phys. Solids 196 (2025) 105963.